SSM/I Rain Retrievals Within an Unified All-Weather Ocean Algorithm

Frank J. Wentz*

Remote Sensing Systems, Santa Rosa, California

Roy W. Spencer

NASA Marshall Space Flight Center, Global Hydrology and Climate Center, Huntsville, Alabama

_____

Corresponding author address: Frank J. Wentz, Remote Sensing Systems, Suite 220, 1101 College Ave. Santa Rosa, California 95404

ABSTRACT

A new method for the physical retrieval of rain rates from satellite microwave radiometers is presented and compared to two other rainfall climatologies derived from satellites. The method is part of a unified ocean parameter retrieval algorithm that is based on the fundamental principles of radiative transfer. The algorithm simultaneously finds near-surface wind speed W, columnar water vapor V, columnar cloud liquid water L, rain rate R, and effective radiating temperature T_U for the upwelling radiation. The performance of the algorithm in the absence of rain is discussed in Wentz [1995], and this paper focuses on the rain component of the algorithm.

A particular strength of the unified algorithm is its ability to 'orthogonalize' the retrievals so that there is minimum cross-talk between the retrieved parameters. For example, comparisons of the retrieved water vapor with radiosonde observations show that there is very little correlation between the water vapor retrieval error and rain rate. For rain rates from 1 to 15 mm/h, the rms difference between the retrieved water vapor and the radiosonde value is 5 mm. A novel feature of the rain retrieval method is a beamfilling correction that is based upon the ratio of the retrieved liquid water absorption coefficients at 37 GHz and 19.35 GHz. This ratio decreases by about 40% when heavy and light rain co-exist within the SSM/I footprint as compared to the case of uniform rain. This correction has the effect of increasing the rain rate when the spectral ratio of the absorption coefficients is small. Even with this beamfilling correction, tropical rainfall is still unrealistically low when the freezing level in the tropics (~ 5 km) is used to specify the rain layer thickness. We restore realism by reducing the assumed averaged tropical rain layer thickness to 3 km, thereby accounting for the existence of warm rain processes in which the rain layer does not extend to the freezing level.

Global rain rates are produced for the 1991 through 1994 period from observations taken by microwave radiometers (SSM/I) that are aboard two polar-orbiting satellites. We find that approximately 6% of the SSM/I observations detect measurable rain rates (R > 0.2 mm/h). Zonal averages of the rain rates show the peak at the intertropical convergence zone (ITCZ) is quite narrow in meridional extent and varies from about 7 mm/day in the winter to a maximum 11 mm/day in the summer. Very low precipitation rates (< 0.3 mm/day) are observed in those areas of subsidence influenced by the large semipermanent anticylones. In general, these features are similar to those reported in previously published rain climatologies (Wilheit *et al.*,1991; Spencer, 1993). However, significant differences do exists between our rain rates and those produced by Spencer (1993). These differences seem to be related to non-precipitating cloud water.

1. Introduction

The accurate retrieval of oceanic rain rates from satellite microwave measurements has been an elusive goal since the concept was first proposed by Buettner (1963), and then demonstrated with satellite data by Wilheit et al. (1977). While the physical basis for these retrievals is sound, we believe that there are three significant assumptions inherent to these methods which make the measurement of tropical average rain rates to better than 10% problematic. These assumptions concern the specification of the following characteristics of a rain system: (1) the rain layer thickness (often assumed to extend from the surface to the freezing level); (2) the relative amount of cloud water versus rain water; and (3) the varying rain intensities across the radiometer footprint (which is commonly called the 'beamfilling effect'). The observed brightness temperature (T_B) is strongly influenced by these three characteristics. Significant new information on these three issues will have to await the Tropical Rain Measurement Mission (TRMM, Simpson et al., 1988), scheduled to be launched in 1998. The combination of TRMM's microwave radiometer and rain radar will help to quantify the above three processes. In the meantime, while the new rain retrieval method described herein does not solve these problems, it does attempt to explicitly address them in a physically realistic way.

We present an unified, all-weather ocean algorithm that simultaneously finds the near-surface wind speed W, columnar water vapor V, columnar cloud liquid water L, rain rate R, and effective radiating temperature T_U for the upwelling radiation. This algorithm is a seamless integration of the Wentz (1995) no-rain algorithm and a newly developed rain algorithm. The algorithm is based on the fundamental principles of radiative transfer and explicitly shows the physical relationship between the inputs (T_B) and outputs (W, V, L, R, and T_U). The wind speed retrieval must be constrained to an *a priori* value for moderate to heavy rain, and T_U must be constrained by a statistical correlation for clear skies and light rain. The other retrieved parameters are unconstrained over the full range of weather conditions. Wentz (1995) discusses the algorithm's performance in the absence of rain, and herein we focus on the rain component of the algorithm.

A particular strength of the new method is its ability to 'orthogonalize' the retrievals so that there is minimum cross-talk between the retrieved parameters. With respect to estimating rainfall, it is important to remove the water vapor contribution to the observed brightness temperature. We will present results showing that the error in retrieved water vapor (as determined from radiosonde comparisons) is uncorrelated to the retrieved rain rate. Likewise, the influence of the radiating temperature T_U is separated from the liquid water signal by using the polarization information that is contained in the observations. Because the rain rates are retrieved only after all other significant influences on T_B are quantified, the various retrievals can be analyzed for climate relationships between them, with high confidence that there is a minimum of algorithm cross-talk.

Conceptually, the rain retrieval involves the following steps. The physics of radiative transfer shows that there is a direct and unique relationship between brightness temperature and the atmospheric transmittance τ_L of liquid water. In view of this, the first step is to directly retrieve τ_L along with the other directly observable parameters W, V, and T_U. In the context of rainfall, τ_L is related to the columnar water in the rain cloud, and T_U provides information on the height from which the radiation is emanating and whether radiative backscattering by large ice particles is occurring (Spencer, 1986). The retrieval of τ_L is done by solving a set of simultaneous brightness temperature equations. A basic premise in this retrieval is that the polarization signature of the

T_B's allows for the separation of the τ_L signal from the T_U signal. The T_B model is formulated such that the T_U parameter includes both radiative scattering effects and air temperature variability. In the next step, the spectral signature of the retrieved τ_L at 19 and at 37 GHz is used to estimate the beamfilling effect. The appropriate beamfilling correction is applied, and the mean atmospheric attenuation A_L for liquid water over the footprint is found. Mie scattering theory and an assumed relationship between cloud water and rain water are then used to convert the A_L to a columnar rain rate (rain rate times column height). Finally, the columnar rain rate is converted to a rain rate by dividing by an assumed rain column height that is a function of a sea surface temperature climatology. In this way, we explicitly handle the three rain cloud characteristics listed above.

The algorithm is developed and tested using the observations taken by the Special Sensor Microwave Imager (SSM/I, Hollinger *et al.,* 1987). The SSM/I is a scanning radiometer that operates at four frequencies: 19.35, 22.235, 37, and 85.5 GHz. It is flown by the Defense Meteorological Satellite Program (DMSP) on two operational polar orbiting platforms. The first in the series of 7 SSM/I's was launched in June 1987. The results herein are based on SSM/I observations for the four year period from 1991 through 1994. Observations from two satellites, F10 and F11, are used. The F10 observations cover the entire 4 year period, while the F11 observations begin in January 1992. The SSM/I time series will probably continue through about the year 2000, at which time it will be replaced by a combined imager/sounder called SSM/IS. Thus there is the opportunity to obtain a 13-year global time series of geophysical products, which can then be further extended with the SSM/IS observations.

The algorithm described herein will be used to produce the NASA Pathfinder Data Set for SMMR and SSM/I. This data set will be a 20-year time series of geophysical parameters, which will be broadly distributed to the research community.

2. Description of the SSM/I

The SSM/I's are carried aboard the DMSP polar orbiters. The orbit for these spacecraft is near-circular, sun-synchronous, and near-polar, with an inclination of 98.8°. The nominal altitude is 860 ± 25 km, and the orbital period is about 102 minutes. The variation in altitude is due to both the eccentricity of the orbit and the oblateness of the Earth. To date, five SSM/I's have been launched aboard the F08, F10, F11, F12, and F13 spacecrafts. Unfortunately, the F12 SSM/I failed. Table 1 gives the launch dates and ascending node times for the remaining four SSM/I's. The ascending node times for F10 and F11 are slowly drifting later into the day. The data from the F08 SSM/I essentially ends in December 1991. Data from the other three SSM/I's are continuing as of December 1995.

The SSM/I sensor consists of 7 separate total-power radiometers sharing a common feedhorn. These 7 radiometers take dual-polarization measurements at 19.35, 37.0, and 85.5 GHz, and just a vertical-polarization measurement at 22.235 GHz. The SSM/I uses an offset parabolic reflector of dimensions 61 by 66 cm to collect the microwave radiation. The reflector focuses the radiation into the corrugated, broad-band, 7-port feedhorn. The reflector and feedhorn spin as a unit about the nadir axis. The rotation period is 1.9 s. A cold-space reflector and a hot reference

Table 1. SSM/I Launch Dates and Ascending Node Times

Satellite	Launch Date	Ascending Node Time
F08	June 1987	6:15 AM
F10	Dec. 1990	8:10 PM to 10:15 PM
F11	Nov. 1991	5:10 PM to 6:30 PM
F13	March 1995	5:45 PM

load are attached to the spin axis and do not rotate. The rotating feedhorn observes the fixed cold reflector and hot load once each scan. In this way, calibration observations are taken every scan.

Earth observations are taken during a 102.4° segment of the rotation. The 102.4° arc is centered on the spacecraft subtrack and corresponds to a 1400-km wide swath on the Earth's surface. The 1400-km swath and the orbit inclination of 98.8° provide complete coverage of the Earth in two to three days, except for two small circular sectors of 2.4° centered on the North and South poles. The nadir angle for the Earth-viewing reflector is 45°, which results in an Earth incidence angle of 53.4° ± 0.25°. The lower frequency channels (19, 22, and 37 GHz) are sampled so that the pixel spacing is 25 km, and the 85 GHz channels are sampled at a 12.5 km pixel spacing. More information on the SSM/I can be found in Hollinger *et al.*(1987) and Wentz (1991).

3. The No-Rain Algorithm

We begin by reviewing the no-rain algorithm described by Wentz (1995). Then Section 4 shows how this algorithm is extended to include rain observations. In the absence of rain, there is a relatively simple and unique relationship between the ocean brightness temperature (T_B) measured by SSM/I and W, V, and L. As a consequence of this simple relationship, these parameters can be retrieved to a high degree of accuracy. The retrieval of (W,V,L) is accomplished by varying their values until the T_B model function matches the SSM/I observations. After a precision calibration to *in situ* observations, the rms retrieval accuracies for W, V, and L are 0.9 m/s, 1.2 mm, and 0.025 mm, respectively (Wentz, 1995). We now give some details on the no-rain algorithm so that one can then see how it is extended to include rain.

The first step in the retrieval process is to average the SSM/I observations to a common spatial resolution. The half-power beamwidths of the SSM/I footprints on the Earth are 56, 44, and 32 km for the 19, 22, and 37 GHz channels, respectively, and the centers of these footprints are coincident. Hence, a 37 GHz observation sees only 33% of the area sampled by the 19 GHz channel. In order to obtain accurate retrievals, it is necessary that all channels see the same ocean area. This is accomplished by averaging the 22 and 37 GHz observations down to the lower resolution of the 19 GHz channel using the following equation:

$$\overline{T}_{AIJ} = \sum_{i=I-1}^{I+1} \sum_{j=J-1}^{J+1} w_{ij} T_{Aij} \tag{1}$$

in which T_{Aij} is antenna temperature (either 22 or 37 GHz) at the original resolution and the two subscripts denote the along-track scan number and the across-track cell position. A set of weights w_{ij} (one for 22 GHz and another for 37 GHz) is found such that the effective antenna pattern of the averaged T_A matches the 19-GHz pattern. The weights depend on the across-track cell position because the relative location of the cells is different at the swath edge as compared to the swath center. The distance between adjacent scans and adjacent cells is approximately 25 km, and we find that it is sufficient to include only the immediately adjacent cells when doing the average. Hereafter, we drop the overbar on T_A, and it is understood that all observations are at a common spatial resolution. Thus, the retrievals are done at a pixel spacing of 25 km, but their actual spatial resolution is about 56 km. Note that for the rain algorithm, the rain rates are computed at the spatial resolution of the 37 GHz footprint, which is 32 km (see Section 6).

The antenna temperatures are then converted to brightness temperatures using the linear transformation given by Wentz (1991). The T_A-to-T_B conversion accounts for the antenna spillover and the cross-polarization leakage. The no-rain algorithm then retrieves three geophysical parameters over the ocean: near-surface wind speed W (m/s), columnar water vapor V (mm), and columnar cloud liquid water L (mm). The retrieval is done by solving the following three model function equations:

$$T_{A22V} = G_{VV}[F_{22V}(W,V,L) + 0.5\Lambda(x)\,\tau_{22}^2\,\Delta T_{BV}]$$

$$+ G_{VH}F_{22H}(W,V,L) + G_{VO}T_{BC} \qquad (2a)$$

$$T_{B37V} = F_{37V}(W,V,L) + 0.9\Lambda(x)\,\tau_{37}^2\,\Delta T_{BV} \qquad (2b)$$

$$T_{B37H} = F_{37H}(W,V,L) \qquad (2c)$$

The SSM/I brightness temperatures at 37 GHz are denoted by T_{B37V} and T_{B37H} for vertical and horizontal polarization, respectively. At 22 GHz, there is only vertical polarization, and the model function equation is in terms of the antenna temperature T_{A22V} rather than brightness temperature. The term T_{BC} is the cosmic background brightness temperature equaling 2.7 K. The G factors are the antenna pattern coefficients that account for antenna spillover and cross-polarization leakage. The values for the G coefficients are given by Wentz (1991). The function F is the isotropic T_B model function. In addition to the explicit arguments W, V, and L, F also depends on sea surface temperature T_S. A sea-surface temperature climatology (Shea *et al.,* 1990) is used to specify T_S.

The terms containing ΔT_{BV} account for the dependence of T_B on wind direction. ΔT_{BV} is the difference between the 19 GHz SSM/I v-pol brightness temperature T_{B19V} minus the isotropic model function and hence is a measure of wind direction variations.

$$\Delta T_{BV} = T_{B19V} - F_{19V}(W,V,L) \qquad (3)$$

The wind direction signal is diminished by the square of the transmittance, τ^2. At low winds for which the wind direction signal is weak, the modeling noise in the retrieval equations is reduced by introducing the term $\Lambda(x)$:

$$\Lambda(x) = 0 \qquad\qquad x < 0 \qquad\qquad (4a)$$

$$\Lambda(x) = 3x^2 - 2x^3 \qquad\qquad 0 \le x \le 1 \qquad\qquad (4b)$$

$$\Lambda(x) = 1 \qquad\qquad x > 1 \qquad\qquad (4c)$$

$$x = (W - 3)/5 \tag{5}$$

$\Lambda(x)$ is a weighting function that smoothly goes from 0 to 1 as its argument x goes from 0 to 1. The coefficients 0.5 and 0.9 in equations (2a) and(2b) are chosen so as to minimize the rms retrieval error.

Equations (2) represent three equations in three unknowns: W, V, and L. These three equations are solved by assuming the equations are stepwise linear in terms of (W,V,L). The analytic derivatives $\partial T_B/\partial W$, $\partial T_B/\partial V$, and $\partial T_B/\partial L$ are computed at a first guess value for (W,V,L). The set of equations is then treated as a linear system with slopes equal to the first guess analytic derivatives, and this set of equations is solved in the usual way using Cramer's rule. The solution gives a new estimate for (W,V,L). The analytic derivatives are then recomputed at the new solution point, and the equations are again solved. This procedure is continued until the difference between the observation and the model function is less than 0.1 K for each channel. Typically 5 iterations are required to reach the 0.1 K convergence level. Although this iterative procedure requires a first guess, it should be emphasized the final solution is independent of the first guess.

4. Extending the Algorithm to Include Rain

To create an all-weather algorithm, the no-rain algorithm is extended in the following ways:

1. The cloud water parameter L is replaced by the total transmittance of cloud and rain water at 37 GHz, τ_{L37}.
2. An additional parameter is added to the retrieval, the cloud and rain transmittance at 19 GHz, τ_{L19}.
3. When rain occurs, the wind speed retrieval is constrained to an *a priori* value.
4. When rain occurs, the effective air temperature T_U for the upwelling radiation becomes a retrieved parameter rather than being specified as a function of retrieved water vapor and climatological sea-surface temperature.

The algorithm extensions are done such that the all-weather algorithm is identical to the no-rain algorithm when there is no rain, and then smoothly transforms to a rain algorithm over the range from very light to moderate rain. Above about 5 mm/h the algorithm no longer retrieves wind speed. The first three modifications are discussed in this section, and the fourth modification involving the effective air temperature is discussed in Section 6.

The first modification is to replace the argument L by the 37-GHz liquid water transmittance τ_{L37} for both cloud and rain water. In the no-rain algorithm, the cloud liquid water L enters the equation only through the transmittance. This dependence can be expressed as

$$\tau = \exp[-\sec\theta\,(A_O + A_V + A_L)] \tag{6}$$

$$A_L = \alpha_L\,[1 - 0.026(T_L - 283)]\,L \tag{7}$$

where θ is the incidence angle, A_O and A_V are the atmospheric oxygen and water vapor absorptions, and A_L is the cloud liquid water absorption. Wentz (1995) gives expressions for A_O and A_V as functions of the effective air temperature and columnar water vapor. In the absence of rain, the radiative transfer through the cloud droplets, which are much smaller than the radiation wavelength, is governed by Rayleigh scattering, and the absorption is proportional to the

columnar liquid water content L (mm) of the cloud (Goldstein, 1951), as indicated by (7). The Rayleigh absorption coefficients α_L are 0.059, 0.078, and 0.208 for 19, 22, and 37 GHz, respectively, when L is in units of millimeters. The absorption has a small dependence on the temperature T_L of the cloud water, which is specified by equation (42) below.

The liquid water dependence in (6) can be equivalently expressed in terms of the liquid water transmittance τ_{LF}:

$$\tau_F \;=\; \tau_{LF} \exp[-\sec\theta\,(A_O + A_V)] \tag{8}$$

$$\tau_{LF} \;=\; \exp(-A_{LF}\sec\theta) \tag{9}$$

The subscript F has been introduced to denote the dependence on frequency. Often it is more convenient to work in terms of the absorption than the transmittance. Given the retrieved value for τ_{LF}, the absorption (before doing the beamfilling correction) is given by

$$A_{LF} \;=\; -\cos\theta\,\ln(\tau_{LF}) \tag{10}$$

When rain is present, the relationship between τ_{LF} and liquid water content is more complex, as discussed in Section 8, and the simple Rayleigh expression is not valid. However, by parameterizing the T_B model in terms of τ_{LF} rather than L, we defer the problem of relating τ_{LF} and liquid water content. In other words, we are dividing the rain retrieval problem into two steps. This first step involves separating the liquid water signal, expressed in terms of τ_{LF}, from the signal of the other parameters. In the second step, a rain rate is inferred from τ_{LF}. It is only in the second step that one is required to make assumptions regarding the beamfilling, the cloud/rain partitioning, and the rain column height.

The second modification is to introduce τ_{L19} as an additional parameter to be retrieved. For the no-rain algorithm, Rayleigh scattering gave a fixed relationship between the 19, 22, and 37 GHz transmittances, and hence it was not necessary to separately retrieve τ_{L19}. However when rain is present there is no fixed spectral relationship between the transmittances. Accordingly, we directly retrieve τ_{L19} by introducing a fourth equation in to the retrieval process. Thus, τ_{L19} and τ_{L37} are retrieved products. The 22-GHz transmittance τ_{L22} is found from an interpolation between τ_{L19} and τ_{L37}, as is discussed below.

The third modification is to eliminate wind speed as a retrieved product when there is significant rain. The decrease in the atmospheric transmittance obscures the surface and degrades the ability to retrieve the wind speed. Furthermore, the T_B modeling error is larger for raining observations due to errors in specifying the effective air temperature, as is discussed in Section 6. For moderate to heavy rain it is best to constrain the wind parameter to some specified *a priori* value. To do this, we use the SSM/I wind retrievals in adjacent, no-rain areas to specify W. If no such wind retrievals are available, we use a monthly, 1° latitude by 1° longitude wind climatology to specify W. This climatology is produced from 7 years of SSM/I observations. The wind direction effect (i.e., ΔT_{BV} terms in (2)) only weakly affects the retrievals and is set to zero for raining observations.

These three modifications result in the following set of retrieval equations:

$$T_{B19V} = F_{19V}(W,V,\tau_{L19}) + 0.9\Lambda(x)[1-\Lambda(y)]\,\tau_{19}^2\;\Delta T_{BV} \tag{11a}$$

$$T_{A22V} = G_{VV}\{F_{22V}(W,V,\tau_{L22}) + 0.5\Lambda(x)[1-\Lambda(y)]\,\tau_{22}^2\,\Delta T_{BV}\}$$

$$+ G_{VH}F_{22H}(W,V,\tau_{L22}) + G_{VO}T_{BC} \tag{11b}$$

$$T_{B37V} = F_{37V}(W,V,\tau_{L37}) + 0.9\Lambda(x)[1-\Lambda(y)]\,\tau_{37}^2\,\Delta T_{BV} \tag{11c}$$

$$T_{B37H} = F_{37H}(W,V,\tau_{L37}) - \Lambda(y)\,[F_{37H}(W_0,V,\tau_{L37}) - T_{B37H}] \tag{11d}$$

The constraint on wind is accomplished by the $\Lambda(y)$ term, which is the weighting function given by (4) above. In this case the argument y is

$$y = (A_{L37} - 0.04)/0.11 \tag{12}$$

Thus $\Lambda(y)$ smoothly goes from 0 to 1 as its argument A_{L37} goes from 0.04 to 0.15. The lower bound for A_{L37}, which represents the onset of rain, was found from an investigation of 38 northeast Pacific extratropical cyclones (Wentz, 1990). This study indicated that when A_{L37} exceeds 0.04, drizzle or light rain is likely. The upper limit represents a rain rate of about 2 mm/h, depending on the rain column height and other factors. When $\Lambda(y) = 0$, the above equations have the same form as the no-rain equations (2). When $\Lambda(y) = 1$, the wind direction term is eliminated, and equation (11d) simply becomes

$$F_{37H}(W,V,\tau_{L37}) = F_{37H}(W_0,V,\tau_{L37}) \tag{13}$$

where W_0 is the *a priori* wind speed. Equation (13) forces the wind retrieval to equal W_0. Thus A_{L37} plays the role of a blending parameter for joining the no-rain algorithm with the raining algorithm. As A_{L37} goes from 0 to 0.15, the algorithm smoothly transforms from the no-rain algorithm to a rain algorithm.

In the no-rain algorithm, Rayleigh scattering gives the following relationship between the 22 and 37 GHz transmittances:

$$\tau_{L22} = \tau_{L37}^{0.375} \tag{14}$$

When rain is present, the Rayleigh relationship is no longer valid, and we use the following interpolation based on the retrieved values of the 19 and 37 GHz transmittances:

$$\tau_{L22} = \tau_{L19}^{0.837}\,\tau_{L37}^{0.163} \tag{15}$$

This interpolation represents a linear interpolation of A_L versus frequency f. According to Mie scattering, the spectral variation of A_L is approximately $f^{1.7}$ for high absorption values. However, the beamfilling effect discussed in Section 7 tends to flatten out the spectral variation of A_L, and a linear variation is found to be a good approximation for moderate to high rain rates. In order to blend the no-rain algorithm with the raining algorithm, the following expression is used to specify τ_{L22} for all values of A_{L37}

$$\tau_{L22} = [(1-\Lambda(z)]\tau_{L37}^{0.375} + \Lambda(z)\tau_{L19}^{0.837}\,\tau_{L37}^{0.163} \tag{16}$$

$$z = 10A_{L37}. \tag{17}$$

Thus for small A_{L37}, τ_{L22} is specified via Rayleigh absorption, and for large A_{L37}, τ_{L22} is specified via the 19-37 GHz interpolation.

The remaining equation to be modified is equation (3) for the 19V T_B wind direction signal ΔT_{BV}. In this equation, the L dependence is specified in terms of the 19 GHz liquid water transmittance τ_{L19}. Since this wind direction term is set to zero for rain rates above about 2 mm/h,

we can use the Rayleigh relationship to specify τ_{L19} as a function of τ_{L37}. Doing this, we obtain the following expression for ΔT_{BV}:

$$\Delta T_{BV} = T_{B19V} - F_{19V}(W, V, \tau_{L37}^{0.286})\tag{18}$$

where $\tau_{L37}^{0.286}$ the Rayleigh transmittance at 19 GHz.

With the above modifications, there are now four equations in four unknowns (W, V, τ_{L19}, and τ_{L37}). This set of equations is solved in the same way as was discussed above for the no-rain algorithm. The equations are assumed to be stepwise linear in terms of (W,V,τ_{L19},τ_{L37}), and the equations are solved in an iterative manner. Typically about 5 iterations are needed to reach the 0.1 K convergence level.

In summary, when it is not raining and A_{L37} is small, the extended algorithm is identical to the no-rain algorithm described by Wentz (1995). Then as A_{L37} increases, the algorithm smoothly transforms to a rain algorithm. The wind estimate is constrained to the *a priori* value, and the fixed Rayleigh relationships among the 19, 22, and 37 GHz transmittances are relaxed, but the same T_B model function is used throughout. In this way, we obtain an unified, all-weather ocean algorithm for SSM/I.

5. Retrieval of Water Vapor in Rain

Figure 1 shows the difference between the SSM/I retrieved water vapor and the value obtained from collocated radiosonde observations (RAOB). The difference is plotted versus rain rate. The quality control of the radiosonde data and the collocation with the SSM/I are discussed in Wentz (1995). There are a total of 35,108 SSM/I overpasses of radiosonde sites. For these overpasses, a total of 81,922 rain observations are found within a 112 km radius of the site. The solid curve shows the mean difference and the dashed curves show the ± one standard deviation of the difference. The rain rate is computed from the SSM/I observations, as described in this paper. The statistics are computed by first binning the observations into 0.5 mm/h rain rate bins. For rain rates between 1 and 15 mm/h, the typical rms difference between the SSM/I and radiosonde vapor is 5 mm. In comparison, the rms difference for the no-rain observations is 3.8 mm. The error analysis in Wentz [1995] indicates that the spatial and temporal sampling mismatch between the SSM/I 56-km footprint and the radiosonde point observation contributes about 3.7 mm to the total rms difference. Thus nearly all of the rms difference for the no rain observations is due to the spatial-temporal mismatch. For the rain observations, about half of the rms difference is due to the spatial-temporal mismatch. The conclusion we draw from Figure 1 is that the retrieval algorithm does provide reasonably good estimates of water in the presence of rain and there is little cross-talk between the vapor retrieval and the rain retrieval.
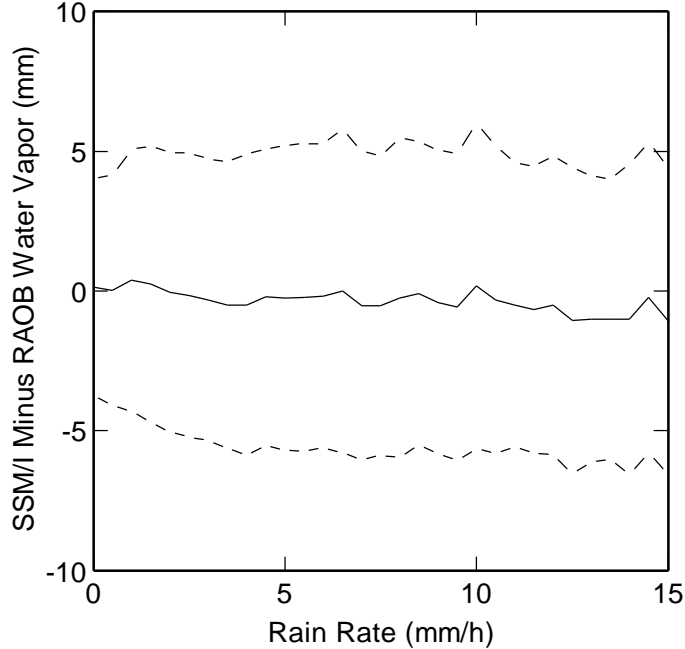
Fig. 1. A comparison of SSM/I and radiosonde columnar water vapor for rainy observations. The solid line is the mean difference, and the dashed lines show the one standard deviation envelope for the differences.

When we first compared the SSM/I and radiosonde water vapor, we found that for large A_{L19}, the SSM/I retrievals were biased low (high) relative to the radiosonde values for high (low) values of sea-surface temperature T_S. In view of this, we apply the following ad hoc correction to the retrieved values of V in order to correct the observed systematic error.

$$V_{corr} \ = \ V_{ret} + 12 \, (T_S - 283) \, (A_{L19} - 0.05)^{1.5} \tag{19}$$

This correction has been applied to Figure 1. We believe that this systematic error is due to radiative scattering and the degradation in the assumed relationship between the effective air temperature and water vapor, as is discussed in the next section. For rain rates above about 10 mm/h, the size of this correction is about 10 mm.

We find that when A_{L19} exceeds about 0.3 (which corresponds to R ~ 15 mm/h, depending on rain column height), the atmosphere is too opaque and/or scattering is too strong to obtain a useful estimate of V. The procedure discussed in Section 6 for obtaining τ_L when radiative scattering is significant requires that V be specified. Thus, for $A_{L19} > 0.3$, we use an *a priori* value for V based on the SSM/I vapor retrievals in adjacent, no-rain and light-rain areas. If no adjacent retrievals are available, we use a monthly, 1° latitude by 1° longitude vapor climatology to specify V. This climatology is produced from 7 years of SSM/I observations.

6. Effective Air Temperature and Radiative Scattering

Implicit in the T_B model function $F(W,V,\tau_L)$ is an assumed relationship for the effective air temperature T_U versus the retrieved columnar water vapor V and a climatological sea-surface temperature T_S. The effective air temperature, which we also call the effective radiating temperature, for the upwelling and downwelling atmospheric radiation are defined as

$$T_U = T_{BU}/(1-\tau) \tag{20a}$$

$$T_D = T_{BD}/(1-\tau) \tag{20b}$$

where T_{BU} and T_{BD} are the upwelling and downwelling atmospheric brightness temperatures and τ is the atmospheric transmittance. An analysis of 42,195 radiosonde observations shows that in the absence of rain T_U and T_D are well correlated with the V and T_S (Wentz, 1995):

$$T_U = \Psi(V,T_S) \tag{21}$$

$$T_D = T_U - c_6 - c_7\, V \tag{22}$$

where the function $\Psi(V,T_S)$ and the coefficients c_6 and c_7 are given by Wentz (1995). At 19 and 37 GHz, T_U and T_D are very similar, with T_U being about 2 K colder.

When rain is present, the accuracy of $\Psi(V,T_S)$. degrades due to two factors. First the process of precipitation and associated convection alters the air temperature. Second, radiative scattering by large rain drops and ice particles reduces T_{BU} and T_{BD}. Since by definition T_U and T_D are proportional to T_{BU} and T_{BD}, they also decrease when scattering occurs. Fortunately, the radiosonde comparisons in the previous section show that the retrieval error in V due to the degradation of $\Psi(V,T_S)$ is not large and can be partially corrected by the ad hoc adjustment (19). However, the error in τ_{L19} and τ_{L37} can be large if scattering effects are ignored.

The effect of radiative scattering on the T_B model is only through the atmospheric parameters τ_L, T_{BU}, and T_{BD}. In view of definitions (20), the T_{BU} and T_{BD} dependence can be equivalently expressed in terms of T_U and T_D. The rain algorithm accounts for scattering (and rain-induced variations in air temperature) by letting T_U become a retrieved parameter rather than being specified by $\Psi(V,T_S)$. Since V and W have been already been found by the procedure described in Section 4, the retrieval problem is reduced to solving the following two equations in two unknowns (i.e., T_U and τ_L).

$$T_{BV} = F_V(T_U,\tau_L) \tag{23a}$$

$$T_{BH} = F_H(T_U,\tau_L) \tag{23b}$$

There is a separate pair of equations for 19 and 37 GHz, and we have temporarily dropped the subscript denoting frequency. Two assumptions are required to solve these equations. First, T_U are T_D are assumed to be closely correlated so that T_D can be specified as a function of T_U, as given by (22) above. The second assumption is that T_U has the same value for vertical and horizontal polarization. In the absence of scattering, T_U is completely independent of polarization. And for moderate to heavy rain, for which scattering is significant, SSM/I observations show that the saturation values for the v-pol and h-pol T_B observations are nearly the same (Spencer et al., 1989). Thus the assumption of polarization independence seems reasonable.

Section 7 gives an example of how equations (23) are inverted to yield τ_L and T_U assuming a simplified T_B model. We denote the solution for T_U for the complete T_B model by the function

$$T_U = \xi(T_{BV}, T_{BH}) \qquad\qquad (24)$$

We use this expression to specify the effective air temperature for the case of moderate to high rain rates. In order to blend this estimate of T_U with the no-rain estimate given by $\Psi(V,T_S)$, we use the following expression:

$$T_U = [1 - \Lambda(u)] \Psi(V,T_S) + \Lambda(u) \, \xi(T_{BV}, T_{BH}) \qquad\qquad (25)$$

$$u = (0.7 - \tau)/0.2 \qquad\qquad (26)$$

and τ is the total transmittance τ of liquid water, water vapor, and oxygen. Equations (23a) and (25) are then combined to retrieve τ_L. When $\tau \geq 0.7$, then $T_U = \Psi(V,T_S)$, and the retrieved τ_L is identical to that found by the no-rain algorithm described in Section 3. When the $\tau \leq 0.5$, the retrieved τ_L and T_U are based solely on the magnitude and polarization signature of the dual-polarization observations (either 19 or 37 GHz). In this way, the all-weather algorithm is identical to the no-rain algorithm for $\tau \geq 0.7$. Then as τ decreases, the equations smoothly transform to a rain algorithm that characterizes the emission and scattering by rain via the τ_L and T_U retrievals, which are based just on the signature of two, dual-polarization observations that have been corrected for water vapor and wind speed effects. Note that $\xi(T_{BV}, T_{BH})$ is inversely proportional to $1 - \tau$, and large retrieval errors occur when $\tau \approx 1$. Thus we only use this method when $\tau < 0.7$. Figure 2 below shows how the accuracy of $\xi(T_{BV}, T_{BH})$ degrades for $\tau > 0.7$.

We define the depression ΔT_U in the effective temperature as

$$\Delta T_U = \xi(T_{BV}, T_{BH}) - \Psi(V,T_S) \qquad\qquad (27)$$

which is a measure of the decrease in brightness temperature due to radiative scattering. In addition to radiative scattering, ΔT_U is also a measure of the decrease in the air temperature due to most of the radiation coming from the cold cloud tops. Figure 2 shows ΔT_U plotted versus τ for the time period from July through September 1992, as derived from the F10 observations. For this time period, the SSM/I retrieval algorithm finds 7,859,295 rain-influenced footprints over the world's oceans. The curves are generated by binning these observations into $\Delta\tau = 0.01$ bins. The solid curves show the mean value for each bin, and the dashed curves show the $\pm$ one standard deviation for each bin. The depression in the effective temperature for the 37 GHz observations, which are most affected by scattering, is about twice that of the 19 GHz observations. For low values of τ, ΔT_U is about -10 K and -20 K for 19 and 37 GHz, respectively. For $\tau > 0.7$, the retrieved value of T_U given by $\xi(T_{BV},T_{BH})$ for 19 GHz becomes noisy and unreliable.

The retrievals W, V, τ_L and T_U are all done at the common spatial resolution of the 19 GHz channels, which is about 56 km, as dictated by equation (1). For the rain rate retrievals, we want as much spatial resolution as possible. In order to obtain a rain rate at the resolution of the 37 GHz footprint, we make the assumption that W and V are uniform over the 19 GHz footprint. The above equations are then used to find τ_{L37} and T_{U37} given the 37-GHz T_B's at their original resolution of 32 km. In Figure 2, the spatial resolution for the ΔT_U values is 56 km for 19 GHz and 32 km for 37 GHz.
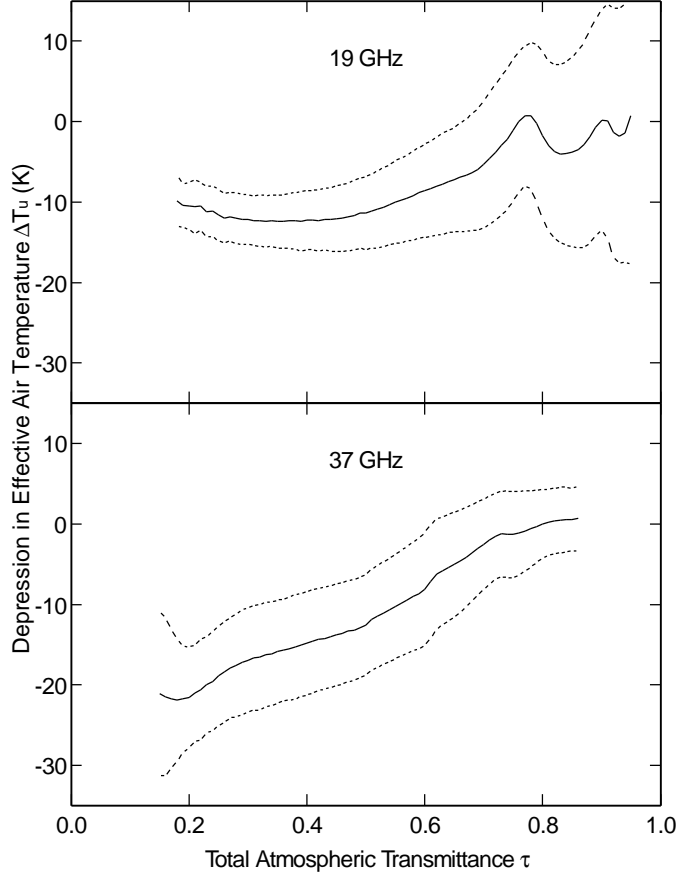
Fig. 2. The decrease in the effective air temperature due to radiative scattering and cold cloud top temperatures.

The beamfilling correction discussed in the next section requires both τ_{L19} and τ_{L37}. Thus to compute a rain rate at the 32-km resolution, a value of τ_{L19} at the spatial resolution of 32-km is required. We use the following expression to specify a high-resolution $\tau_{L19,HI}$

$$\ln(\tau_{L19,HI}) = \ln(\tau_{L19}) \left[\ln(\tau_{L37,HI}) / \ln(\tau_{L37})\right] \tag{28}$$

where the subscript HI denotes the higher spatial resolution. Note that (28) is in terms of the absorption, i.e., $\ln(\tau_L)$. The assumption behind equation (28) is that, even though the cloud and rain water may significantly vary over the footprint, the ratio of 19-to-37 GHz liquid water absorption is relatively constant. If this is true, then the observed spatial variation in τ_{L37} can be used as a scaling factor to compute τ_{L19} at the higher spatial resolution. In reality, this spectral ratio will have some inter-footprint variability, and (28) will introduce some error into the rain retrieval. However, this error will tend to be unbiased and will tend to zero when doing spatial and temporal averages of rain rate.

7. The Beamfilling Effect

The terminology 'beamfilling effect' refers to the non-linear relationship between rain rate R and brightness temperature T_B that occurs when averaging over the radiometer footprint. To illustrate this effect, we use a relatively simple model for the brightness temperature:

$$T_B = T_E(\tau)(1 - \tau^2 R) \tag{29}$$

where $T_E(\tau)$ is the effective temperature of the combined ocean and atmosphere system, τ is the total transmittance through the atmosphere, and R is the reflectivity of the sea surface. The effective temperature is a function of τ. For $\tau = 1$, T_E equals the sea surface temperature T_S, and for $\tau = 0$, T_E equals the effective temperature T_U of the upwelling atmospheric radiation. T_E smoothly varies from T_S to T_U as τ goes from 1 to 0.

Despite its simplicity, equation (29) is actually a very good approximation to the complete T_B model function described in Section 3 and provides considerable insight into the retrieval algorithm discussed in the previous sections. As discussed in Section 6, to separate τ from the T_E signal requires dual-polarization observations, either at 19 or 37 GHz. Looking at the simple T_B model above, we see that the T_E term is easily eliminated, and the transmittance given by

$$\tau^2 = \frac{T_{BV} - T_{BH}}{R_H T_{BV} - R_V T_{BH}} \tag{30}$$

Values for the wind speed and water vapor come from the procedure discussed in Section 4. The wind speed and climatology sea-surface temperature are used to specify R_V and R_H. The oxygen and water vapor components of τ^2 are factored out using equation (8), thereby obtaining just the liquid water transmittance τ_L^2. This method of using polarization information to separate the τ signal from the T_E signal is similar to that proposed by Petty (1994).

We see that for rain retrievals the basic observable is τ_L^2, which represents an average value over the SSM/I footprint. Using equation (9), the footprint average is given by the following integral

$$\tau_L^2 = \int e^{-2A' \sec\theta} P(A')dA' \tag{31}$$

where the integral is over the probability density function $P(A')$ for the cloud and rain water absorption A' within the footprint. The desired retrieval is the mean absorption over the footprint, which is given by

$$A_L = \int A' P(A')\,dA' \tag{32}$$

Without any correction for the spatial averaging, the estimate of the absorption would be

$$\hat{A}_L = \frac{-\ln \tau_L}{\sec\theta} \tag{33}$$

Any variation of the absorption within the footprint will result in the estimate $\hat{A}_L$ being lower than the true mean value A_L. This systematic underestimation of the absorption is called the beamfilling effect.

If $P(A')$ is an exponential distribution of the form

$$P(A') = \frac{e^{-\left(\frac{A'}{A_L}\right)}}{A_L} \qquad \text{34)}$$

then the integrals in (31) and (32) are easily evaluated, and one obtains the following relationship between A_L and $\hat{A}_L$:

$$A_L = \frac{e^{2\hat{A}_L\beta^2 \sec\theta} - 1}{2\beta^2 \sec\theta} \qquad (35)$$

$$\beta = \frac{\Delta A_L}{A_L} \qquad (36)$$

ΔA_L is the rms variation of A' within the footprint and β is the normalized rms variation of A'. For an exponential distribution β equals unity. An expansion of statistical moments shows that, to the second order in $\hat{A}_L\beta^2$, (35) is correct for any distribution $P(A')$ having a mean A_L and an rms variation of ΔA_L. Thus if β is known, (35) can be used to correct the beamfilling effect. β is a normalized quantity that is related to the variability of liquid water in the footprint and hence is essentially independent of frequency.

In order to find β, we note that the ratio $\hat{A}_{L37}/\hat{A}_{L19}$ will be less than that predicted by Mie scattering theory when the beamfilling effect is significant. Thus comparing $\hat{A}_{L37}/\hat{A}_{L19}$ to the Mie absorption ratio provides the means to determine the beamfilling effect. The relationship between the Mie ratio and $\hat{A}_{L37}/\hat{A}_{L19}$ is given by the 37-to-19 GHz frequency ratio of equation (35):

$$\frac{A_{L37}}{A_{L19}} = \frac{e^{2\hat{A}_{L37}\beta^2 \sec\theta} - 1}{e^{2\hat{A}_{L19}\beta^2 \sec\theta} - 1} \qquad (37)$$

where the left-side is the Mie ratio given by equation (40) below. This ratio varies from 3.5 for light absorption values to 2.8 for heavy absorption. If the beamfilling effect is not significant, then $\hat{A}_{L37}/\hat{A}_{L19}$ will equal A_{L37}/A_{L19}. (Because of retrieval error, $\hat{A}_{L37}/\hat{A}_{L19}$ is sometimes slightly greater than A_{L37}/A_{L19}.) Thus when $\hat{A}_{L37}/\hat{A}_{L19} \geq A_{L37}/A_{L19}$, no beamfilling correction is done (i.e., β is set to 0). Otherwise (37) is inverted to find β as a function of the two ratios: $\hat{A}_{L37}/\hat{A}_{L19}$ and A_{L37}/A_{L19}. The inversion is readily done because the expression on the right-side of (37) increases monotonically with β. It equals $\hat{A}_{L37}/\hat{A}_{L19}$ when $\beta = 0$. Thus, the beamfilling correction consists of finding a value for β that when substituted into (37) yields the absorption ratio given by the Mie theory. Given β, the mean absorption for the footprint is then found (35). Since the Mie ratio depends on A_{L37}, an iterative procedure is required to find β. However, the iterative process quickly converges to a unique solution for β because A_{L37}/A_{L19} only weakly depends on A_{L37}.

The magnitude of the beamfilling correction is characterized in terms of the ratios $A_{L19}/\hat{A}_{L19}$ and $A_{L37}/\hat{A}_{L37}$, which are called the beamfilling correction factors (BCF). When $\hat{A}_{L37}/\hat{A}_{L19}$ is significantly less than A_{L37}/A_{L19}, large values for β and BCF are found. For example, when $\hat{A}_{L37}/\hat{A}_{L19} = 2$, the BCF is 1.4 and 2.0 for 19 and 37 GHz respectively. For even smaller values of $\hat{A}_{L37}/\hat{A}_{L19}$, the BCF increases exponentially, and we must impose the following limits. The maximum values of 3.4 and 6.4 are used for the 19 and 37 GHz BCF, respectively, which corresponds to the exponent $2\hat{A}_{L37}\beta^2\sec\theta$ in (35) reaching a value of 3.0. If the BCF exceeds the maximum, it is reset to the maximum. Another overall limit is placed on A_{L19} and A_{L37}. Neither

values is allowed to exceed 1.2. These limits correspond to observations of heavy rain for which the 37 GHz and, to a lessor degree, the 19 GHz brightness temperatures have reached saturated levels. The effect of these limits is to place an upper bound on the retrieved rain rate. For the extreme case of A_{L19} reaching a value of 1.2, the retrieved rain rate will be about 25 mm/h (75 mm/h) for a rain column height of 3 km (1 km). We consider the 25 mm/h limit as an extreme upper bound on the SSM/I's ability to retrieve rain. For such high rain rates, both the 19 and 37 GHz observations have saturated, and the retrieval error can be very large. A more conservative approach would be to lower the limit to 15 or 20 mm/h (for a 3 km column height).

Figure 3 shows the 37-GHz absorption plotted versus the 19-GHz absorption for the July through September 1992 period discussed in Section 6. The bottom curve in Figure 3 shows the retrieved absorptions $\hat{A}_{L37}$ versus $\hat{A}_{L19}$ before the beamfilling correction. The middle curve shows the absorptions A_{L37} versus A_{L19} after the beamfilling correction, and the top curve shows the theoretical curve computed from Mie scattering computations. The curves are generated by binning the 7,859,295 observations into absorption bins having a width of 0.005. The solid curves show the mean value for each bin, and the dashed curves show the ±1 standard deviation for each bin. The A_{L37} versus A_{L19} curve closely follows the theoretical curve up to values of A_{L19} ≈ 0.4. Above this value, the restriction that $A_{L37} \leq 1.2$ becomes important, and the curve asymptotically tends to the 1.2 value. For the high absorption bins, A_{L37} is a constant 1.2, and hence standard deviation envelope goes to zero.

Figure 4 shows the effect of the normalized rms variation β on the computation of A_{L37} and A_{L19}. For this figure, equation (35) is used to compute A_{L37} and A_{L19} from the retrieved values $\hat{A}_{L37}$ and $\hat{A}_{L19}$ using for four different β values: 0.7, 0.8, 0.9, and 1.0. That is to say, rather than computing β for each observation, we use an average value. The theoretical Mie curve lies between the $\beta=0.8$ and $\beta=0.9$ curves. This indicates that, on the average, the beamfilling effect is characterized by a normalized rms variation $\beta \approx 0.85$, which is somewhat less than the $\beta = 1$ value given by an exponential probability density function for A_L.

8.   Inferring Rain Rate from Liquid Water Attenuation

In this section we describe how rain rate is inferred from the retrieved values of A_{L19} and A_{L37} once the beamfilling correction has been applied. The retrieval method discussed above results in A_L being directly related to the transmittance τ of the radiation from the sea-surface up through the atmosphere. Thus, more generally speaking, the retrieved A_L is an attenuation factor for the polarized sea surface signal traveling from the sea-surface upward through the atmosphere. In the absence of scattering, the attenuation and absorption are equivalent and are given by

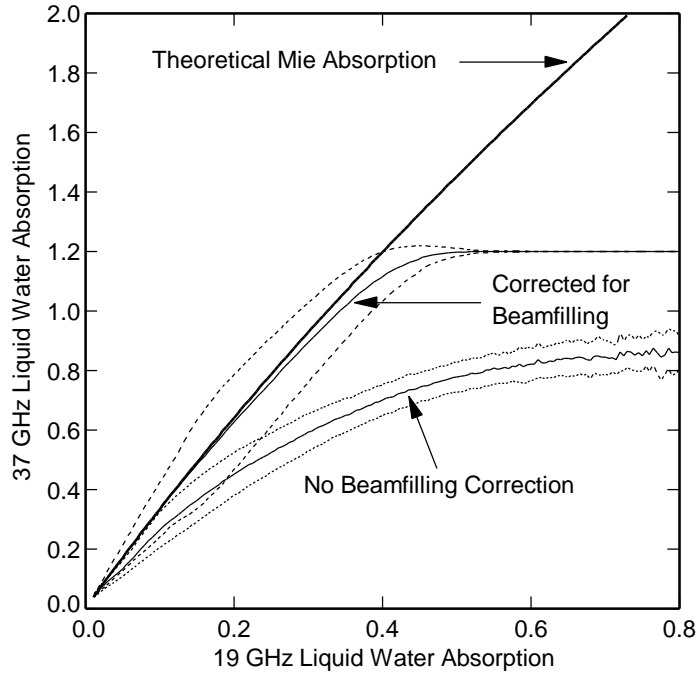$$A_L = \int_0^H \kappa(h)dh \qquad (38)$$

Fig. 3. The decrease in the observed 37-to-19 GHz absorption ratio due to the beamfilling effect.
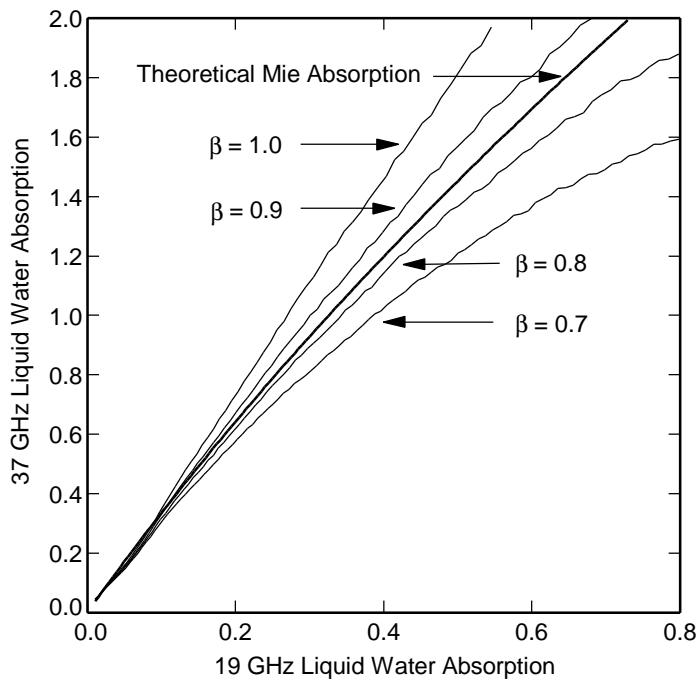

Fig. 4. Parametric curves showing the effect of the normalized spatial variability β of liquid water on the 37-to-19 GHz absorption ratio.

where the integral is over altitude h (km), $\kappa(h)$ (km^{-1}) is the Mie absorption coefficient, and H (km) is the height of the liquid water column. Radiative scattering from rain drops and ice modify the attenuation. For example, the attenuation for point-to-point microwave communication links is still given by (38), but $\kappa(h)$ is the Mie extinction coefficient, rather than absorption coefficient. However, the sea surface is an extended source, as opposed to a point source. For an extended source, the polarized surface signal traveling along the SSM/I viewing direction is scattered in other directions, while the surface signals traveling in other directions are scattered into the SSM/I viewing direction. These two effects tend to compensate, and using the extinction coefficient in (38) would overestimate the attenuation of the surface signal.

For moderate to heavy rain (R $\geq$ 10 mm/h), the 19 GHz (37 GHz) extinction coefficient is about 20% (60%) higher than the absorption coefficient. One distinguishing characteristic between the extinction and absorption coefficients is their spectral signature. For light to moderate rain (5 mm/h) the 37-to-19 GHz ratio for the extinction coefficient is 3.8 as compared to 3.0 for the absorption coefficient. Figure 3 shows the spectral signature of the SSM/I retrieved $\hat{A}_{L37}/\hat{A}_{L19}$ is about 2 for light to moderate rain. Thus, a significantly larger beamfilling correction would be needed for the extinction coefficients as compared to the absorption coefficients. We decided to use the absorption coefficient to evaluate (38) because 1) its spectral signature is closer to the observed $\hat{A}_{L37}/\hat{A}_{L19,}$ and 2) we expect that the attenuation of the polarized surface signal due to scattering will be small (i.e., the scattering in to and out of the viewing direction will tend to cancel).

Fortunately, the choice of the attenuation coefficient does not have a large effect on the retrieved rain rate. The larger extinction coefficients would give a lower rain rate except for the fact that the beamfilling correction is larger for the extinction coefficients. These two factors tend to cancel each other, and, in general, the rain retrievals using the absorption coefficients are only about 10% higher than using the extinction coefficients. For example, if the best choice for κ in (38) is halfway between the absorption and the extinction coefficient, then our rain retrievals would be biased about 5% high.

The Mie absorption coefficient for a rain cloud is found by integrating the Mie absorption cross sections (Born and Wolf, 1975) over the drop size distribution for the rain cloud, as described by Wilheit *et al.* (1977). The drop size distribution is partitioned into two parts: the non-precipitating cloud water and the falling rain water.

$$\kappa = \int N_C(r)\sigma(r)dr \; + \; \int N_R(r)\sigma(r)dr \qquad (39)$$

where r is the drop radius, $N_C(r)$ and $N_R(r)$ are the drop size distributions for cloud and rain water, respectively, and $\sigma(r)$ is the Mie absorption cross section. When r is much smaller than the radiation wavelength, which is the case for the cloud water integral, $\sigma(r)$ is simply proportional to r^3, and as a result the cloud integral is proportional to the total volume of cloud water per unit volume of atmosphere. Thus the vertically integrated cloud absorption given by (38) is proportional to the columnar cloud water L.

For the rain integral, the simple $\sigma(r) \propto r^3$ does not hold, and the absorption depends on the details of the drop size distribution. We use the Marshall and Palmer (1948) drop size distribution to specify $N_R(r)$. The Marshall-Palmer distribution is parameterized in terms of a nominal rain rate. Following the method described by Wilheit *et al.* (1977), we vary this nominal rain rate from

0.01 to 50 mm/h and compute the above rain absorption integral, denote by κ_R, and the actual rain rate R assuming the fall velocity given by Waldteufel (1973). We find that the κ_R versus R relationship in the 19-37 GHz band is well approximated by a power law relationship, which is close to linear.

Combining (38) and (39) gives

$$A_{L19} = 0.059(1 - 0.026\Delta T)L + 0.0122(1 + 0.004\Delta T)HR^{1.06} \tag{40a}$$

$$A_{L37} = 0.208(1 - 0.026\Delta T)L + 0.0436(1 - 0.002\Delta T)HR^{0.95} \tag{40b}$$

$$\Delta T = T_L - 283 \tag{41}$$

where L is the columnar cloud water (mm), R (mm/h) is the rain rate averaged over the rain column, and H is the height of the rain column. There is a small dependence on the rain cloud temperature T_L. The mean temperature between the surface and the freezing level is used to specify T_L.

$$T_L = (T_S + 273)/2 \tag{42}$$

where T_S is the climatology sea-surface temperature.

Equation (40) reveals a fundamental problem in retrieving rain rate. Given just A_{L19} and A_{L37}, it is not possible to uniquely separate and retrieve L, R, and H. The spectral dependencies of the cloud water term and the rain rate term are nearly the same, as can be seen by the spectral ratio of the coefficients (0.208/0.059 = 3.5;.436/0.0122 = 3.6). And, by doubling the rain rate R and halving the height H, one obtains about the same A_L. Thus to obtain an estimate for R, one must make *a priori* assumptions regarding L and H. Potentially, these assumptions can produce significant errors in the rain retrievals.

We know little of the statistics of cloud water versus rain rate in rain clouds. The data presented by Pruppacher and Klett (1980) indicate that heavy rain clouds can have values of L on the order of 1 to 2 mm. It seems reasonable to assume that, in general, L increases with R and then tend to level off at very high rain rates. Furthermore, an investigation of 38 northeast Pacific extratropical cyclones (Wentz, 1990) indicates that when the SSM/I retrieval of L reaches a value of 0.18 mm, a drizzle or light rain is likely. The following expression incorporates the features of 1) rain beginning at L = 0.18 mm, 2) L increasing with R, and 3) the L versus R relationship leveling off at high R, with L reaching a maximum value between 1 and 2 mm.

$$L = 0.18\left(1 + \sqrt{HR}\right) \tag{43}$$

The specification of the rain column height H is based, in part, on the altitude H_F of the freezing level as derived from the radiosonde observations. The global radiosonde observations for the 1987-1990 period collected by Wentz (1995) are used to find H_F as a function of the sea-surface temperature T_S. Out of the total 42,195 radiosonde soundings, we only use the 9,120 soundings for which the surface relative humidity is $\geq$ 90%. By restricting the data set to high humidity cases, the results should be more indicative of rain observations. Figure 5 shows the height of the freezing level measured by the radiosondes versus the climatological sea surface temperature at the radiosonde site. For the stations at very high latitudes, the typical value of H_F is about 1 km. The mid-latitude value of H_F ranges from 2 to 4 km, and in the tropics H_F reaches a value of 5 km.

Equation (40) shows that the retrieved rain rate is very nearly proportional to H^{-1}. Thus the proper specification of H is critical to obtaining good rain rate retrievals. In a preliminary analysis, we used the H_F values shown in Figure 5 to specify H and found that the rain rates in the tropics were about 40% low in comparison to other climatologies (see Section 9). We attribute at least part of this systematic underestimation to cases for which the rain column does not extend the full 5 km to the freezing level. In general, H_F is an upper bound on H, and there will be many cases for which $H < H_F$. Thus using H_F will, on the average, tend to underestimate the rain rate. If there is a substantial amount of rain in the tropics that forms without an ice phase (Fletcher, 1969) then the underestimation will be large.

In the tropics, we find that using H = 3 km, rather than the 5-km freezing level, corrects the underestimation of rain relative to other climatologies. We believe that the assumption of a mean column height of 3 km is not unreasonable and may be an indication of the prevalence of warm rain processes in the tropics. Outside the tropics, we use H_F to specify H. The following simple regression, which is shown in Figure 5, is derived so as to match H_F for low values of T_S and to reach a value of 3 km for high values of T_S.

$$H = 1 + 0.14(T_S - 273) - 0.0025(T_S - 273)^2 \qquad T_S < 301 \qquad (44a)$$

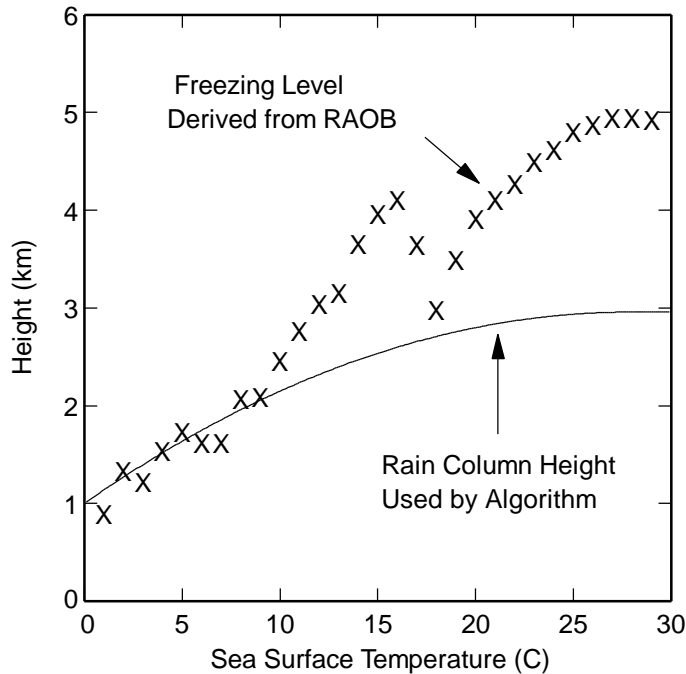$$H = 3 \qquad T_S \geq 301 \qquad (44b)$$

Fig. 5. The altitude of the atmospheric freezing level plotted versus the climatology sea surface temperature.

Having specified H and the relationship between R and L, one can invert equation (40) and find a value for R given A_L. Note that as a result of the beamfilling correction discussed in Section 7, the retrieved values of A_{L19} and A_{L37} are not independent. Rather they are computed such that their ratio is consistent with equation (40) above. For this reason, the same value for R is found from either A_{L19} or A_{L37}. The one exception is when A_{L37} exceeds the maximum value of 1.2. In this case, A_{L19} is used to compute the rain rate.

9. Rain Retrieval Results

a. Probability density function of SSM/I rain rates

All results in this section are based on SSM/I observations for the four year period from 1991 through 1994. Observations from two satellites, F10 and F11, are used. The F10 observations cover the entire 4 year period, while the F11 observations begin in January 1992. The top frame in Figure 6 shows the probability density function (pdf) for the rain rates inferred from the two SSM/I's. The thick curve shows global results, and the thin curve shows tropical results (20S to 20N). The computation of any rain pdf is very dependent on the temporal and spatial averaging. For the SSM/I, the temporal averaging is essentially instantaneous, and the spatial averaging has a resolution of about 32 km. A rain pdf computed from rain gauges looks very different than that shown in Figure 6 because the spatial averaging is very different. The leftmost point on the pdf curves corresponds to the number of no-rain observations. A total of 85.9% of the SSM/I observations indicated no rain. An additional 8.3% of the observations indicated very light rain not exceeding 0.2 mm/hr, and the remaining 5.8% of the observations indicate rain exceeding 0.2 mm/hr. We consider the accuracy of the 'very light rain' retrievals as questionable. Some or many of these observations may actually be heavy non-raining clouds. Note that the contribution of the very light rain observations to the total rainfall is very small (see below).

To determine the contribution of the various footprint-averaged rain rates to the overall rainfall amount, we multiply the rain pdf by the rain rate, as shown in the bottom frame in Figure 6. In this case, the area under the curve equals the average oceanic rainfall, which is 0.12 mm/hr (2.9 mm/day) globally and 0.16 mm/day (3.9 mm/day) in the tropics. The questionable very light rain observations (R < 0.2 mm/h) only contribute 0.007 mm/h (0.17 mm/day) to this total. One-half of the total global oceanic rainfall occurs at footprint-averaged rates above (and below) about 3.5 mm/h. For rainfall in the tropics, this value increases to 5.5 mm/h. Due to the large size of the footprint (32 km) over which the enveloped rainfall is averaged, this mid-point value is much lower than that obtained from rain gauges. Four-minute rain gauge statistics (Jones and Sims, 1978) suggest that about half of tropical rainfall occurs at rates above about 20 mm/h. One possible interpretation of this result is that, on the average when significant rain is being observed, only about one quarter of the SSM/I footprint is actually covered by rain.

b. Global distribution of SSM/I rain rates

Figure 7 shows the seasonal and annual zonally averaged rainfall computed from the SSM/I observations for 1991 through 1994. The meridional structures revealed by the SSM/I are similar to previously published climatologies. The maximum oceanic rainfall occurs at the equatorial latitudes associated with the strong convection in the intertropical convergence zone (ITCZ) for all seasons. This peak is quite narrow in meridional extent and varies from about 7 mm/day in the winter to a maximum 11 mm/day in the summer. The seasonal north-south migration of the

ITCZ, which is in phase with the solar insolation, is also apparent in the figure. The extratropical rainfall is greater in the northern hemisphere than in the southern hemisphere for all seasons. Low precipitation rates (~ 1 mm/day) are observed in those zones of subsidence influenced by the large semipermanent anticylones.

Figure 8 shows color-coded global maps of the SSM/I annual and seasonal rainfall average over the four years from 1991 through 1994. The major features of the spatial distribution of the average annual rainfall are quite similar to those revealed in other satellite climatologies (see below). The largest annual rainfall amounts are seen to occur in the tropical Pacific, extending from South America to Papua New Guinea. Peaks of 15 mm/day occur throughout this band. Additional heavy rain associated with the Indian summer monsoons is apparent in the Bay of Bengal. The other major feature of the global rainfall maps is the extremely dry areas associated with the large semipermanent anticylones in the Southeast Pacific and Southeast Atlantic. These areas are essentially void of rain (R < 0.3 mm/day).
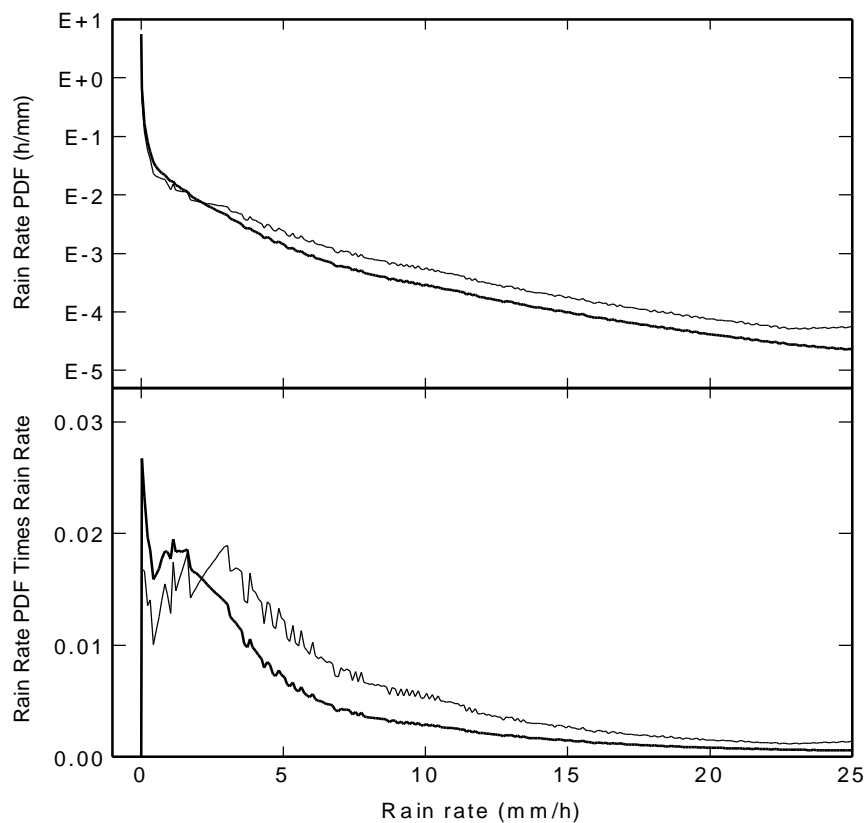

Fig. 6. The top frame show probability density function (pdf) for rain rate averaged over the SSM/I footprint. The bottom frame show the rain pdf times the rain rate. The thick curves show global results, and the thin curves show tropical results.
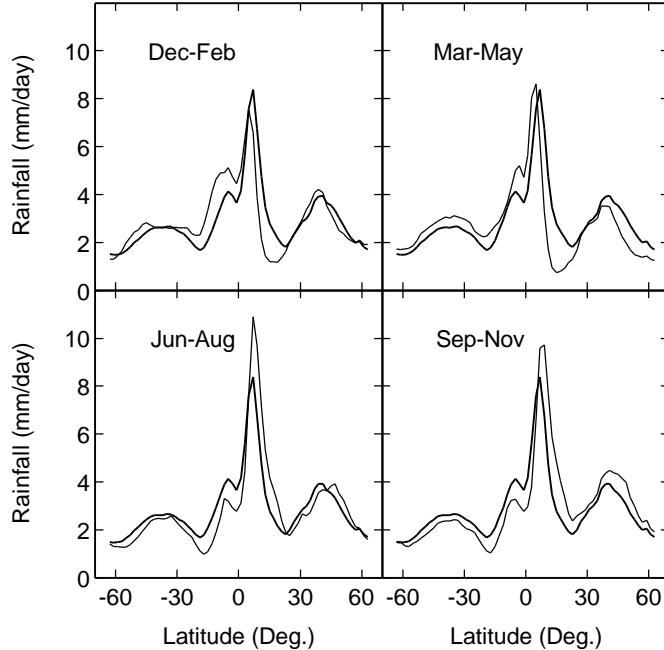
Fig. 7. The zonal average of rainfall over the ocean. The thick curve, which is repeated in each frame, is the annual average. The thin curve is the 3-month seasonal average.

c. Comparison to other satellite climatologies

We now compare our rainfall estimates (hereafter "WS") to two other emission-based rain climatologies: Spencer (1993; hereafter "MSU"), and Wilheit *et al.* (1991; hereafter "WCC"). The MSU rain rates are inferred from the 50.3 GHz T_B observations taken by the Microwave Sounding Unit (MSU). The WCC rain rates are inferred from the SSM/I T_B observations. The same period of record (1991-1994) is used from these data sets. Figure 9 compares the three estimates of the annual zonally averaged rainfall. In general, the three rainfall estimates are similar, but there are some notable differences. We first note that above 50N and below 55S, the MSU rain data are contaminated by sea ice (see below). This explains the upturn at the two ends of the MSU curve in Figure 9. In the ITCZ, the WS, MSU, and WCC reach maximum values of 8.1, 7.4, and 6.9 mm/day, respectively. This represents about a 15% difference between the highest estimate (WS) and the lowest estimate (WCC). In the extratropics storm track regions, the situation changes. Here the WS rainfall is the lowest, and MSU is the highest. Very close agreement is seen in the very dry areas associated with the semipermanent anticylones.

Figure 10 shows color-coded global maps of the MSU minus WS rainfall and the WCC minus WS rainfall. To compute these differences, the rainfall is averaged over the four years (1991-1994) and then smoothed to a spatial resolution of about 300 km. The largest differences are seen between the MSU and WS. The MSU produces more rainfall in the downstream portions of the extratropical storm tracks, and less rainfall over most portions of the tropics, particularly in the tropical west Pacific. Comparisons of Figure 10 to SSM/I retrievals of cloud water (not shown) suggest that the MSU-WS differences might be related to cloud water. Areas where the
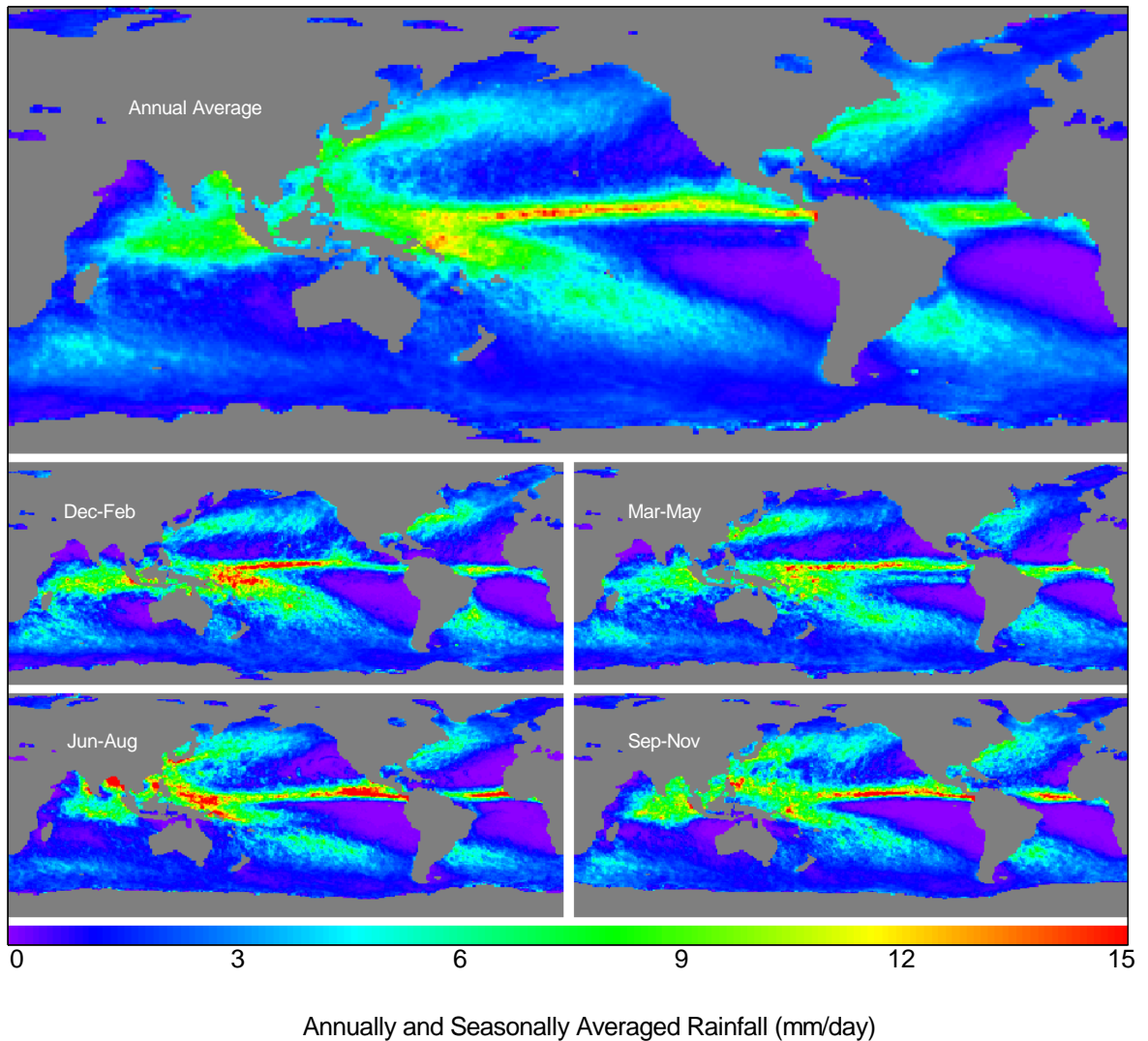
Fig. 8. Average rainfall for 1991 through 1994 derived from SSM/I. The top map shows the annual rainfall, and the four smaller maps show the seasonal averages.

MSU-WS difference is significantly positive (negative) are moderately correlated with areas having a relatively high (low) cloud amount as compared to the rainfall. One example is the downstream portions of the extratropical storm tracks where there is significant cloud coverage but relatively little rain. In these regions the MSU rainfall is about 2 mm/day higher than WS. In contrast, along most of the ITCZ, the cloud content is relative small compared to the heavy rain, the MSU rainfall is about 2 to 3 mm/day lower than WS. An interesting ocean area is seen just west of Central America and Columbia. The north (south) part of this area shows large negative (positive) MSU-WS differences. An analysis of SSM/I retrievals shows moderately heavy rain
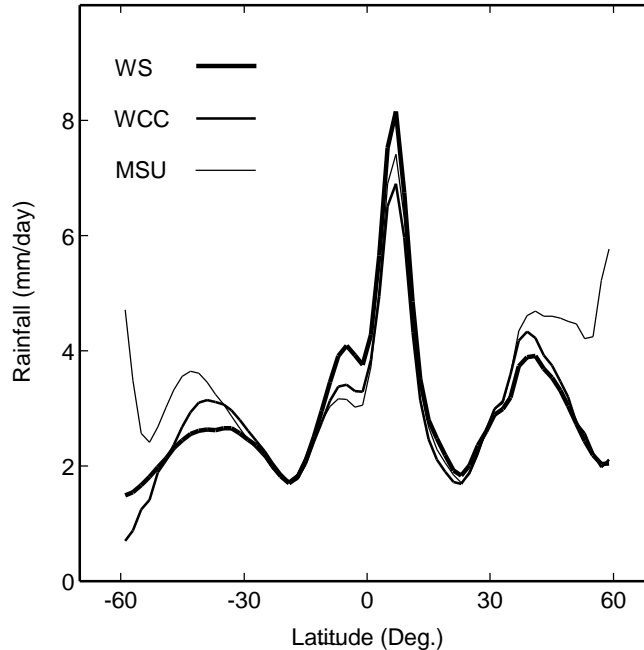
Fig. 9. A comparison of zonally averaged rain rates from three satellite climatologies. WS denotes our results, WCC denotes the Wilheit et al. (1991) results, and MSU denotes the Spencer (1993) results. The upturn at the two ends of the MSU curve is due to sea ice contamination.

and relatively small cloud contents in the north and the reverse situation in the south, which is the same correlation as seen in the storm tracks and the ITCZ. The correct partitioning of cloud and rain water is a problem for both MSU and SSM/I. As pointed out by Spencer (1993), the hypersensitivity of the MSU 50.3 GHz channel to both cloud water and rain water makes the MSU unable to distinguish between the two. We have somewhat more confidence in the SSM/I rainfall because the frequencies of 19.3 and 37 GHz are less sensitive to cloud water, and we have attempted to do a cloud versus rain partitioning. This confidence is bolster by the fact that the cloud-to-rain ratio derived from SSM/I seems realistic. It is a minimum just off the east coasts of the continents where baroclinic wave activity is the strongest. Then this ratio increases eastward across the ocean basins, consistent with weaker wave activity.

The difference map between WS and WCC shows better agreement. The major difference is in tropical areas of heavy rain, where the WS is about 2 mm/day higher. In the extratropical storm tracks, the WCC is typically about 1 mm/day higher. In the dry areas, all three rain estimates (WS, MSU, and WCC) agree well. We find no obvious correlation between the WS-WCC difference and other parameters, except for the rainfall itself. When the rain is very heavy, WS tends to be higher than WCC.

Note that in the WS-MSU figure, the red areas in Sea of Okhotsk, the Bering Sea, Hudson Bay, Labrador Sea, and off Antarctica are sea ice contamination in the MSU rain product. A very small amount of ice contamination is also seen in the WCC product just north of Japan.

Difference in Rainfall for the 1991 Through 1994 Period (mm/day)
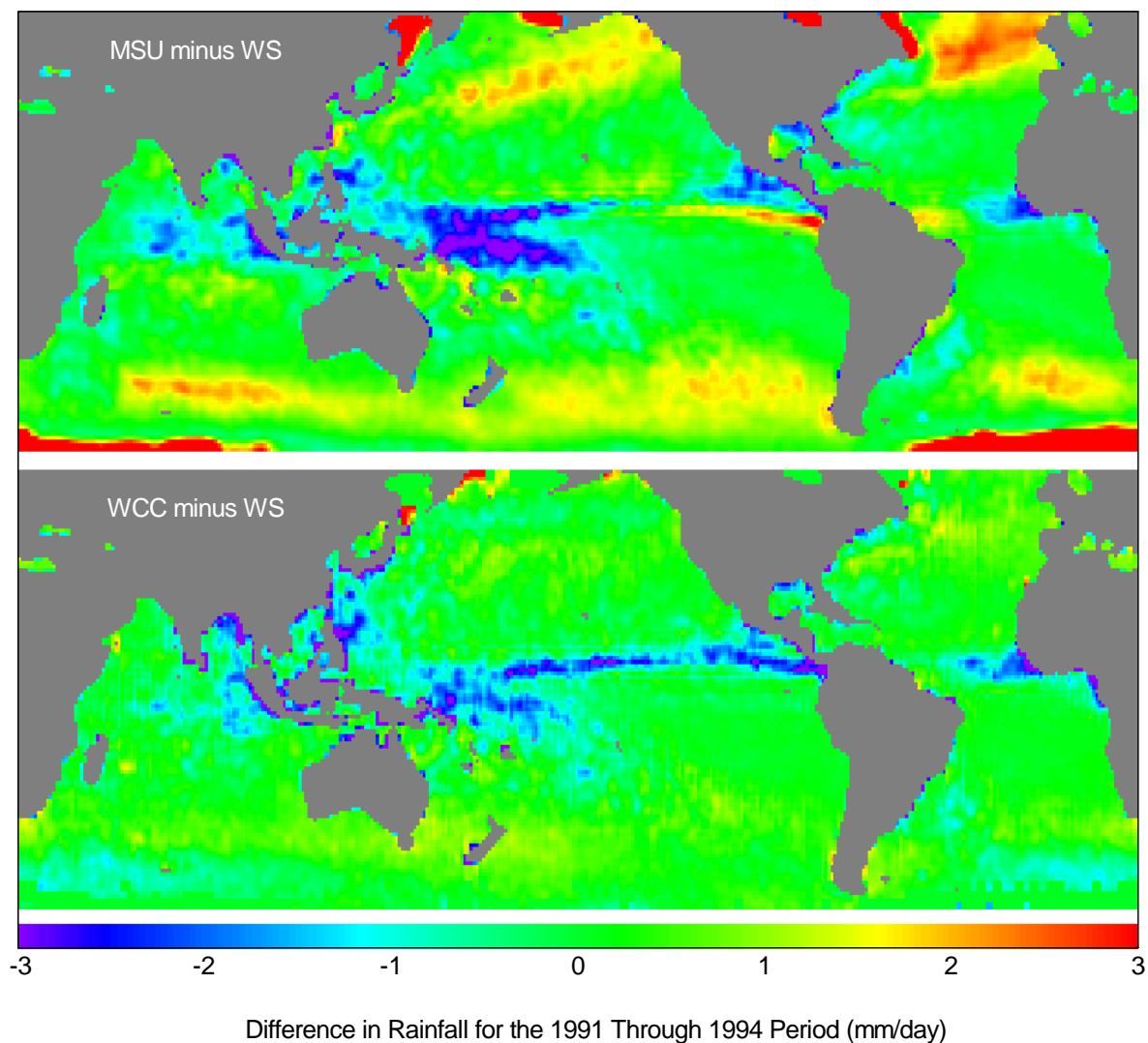
Fig. 10. A comparison of three satellite-derived rain maps. The top image shows the rainfall derived from the MSU (Spencer 1993) minus the SSM/I rainfall computed from the algorithm described herein (WS). The bottom image shows the rainfall produced by the Wilheit et al. (1991) algorithm (WCC) minus the WS rainfall.

10. Conclusions

A new method for the physical retrieval of rain rates from the SSM/I has been presented and compared to two other microwave emission-type rainfall climatologies. The method is part of a unified ocean parameter retrieval algorithm that also diagnoses total integrated water vapor, cloud water, and wind speed. The algorithm first retrieves those geophysical parameters directly observed by SSM/I. With respect to rain, the two relevant parameters are the liquid water

transmittance τ_L and its corresponding effective radiating temperature T_U. A beamfilling correction is then applied based on the spectral signature of the retrieved τ_L at 19 and at 37 GHz. Finally assumptions about the cloud versus rain water partitioning and the rain column height are made to obtain a value for rain rate.

We find that the water vapor retrievals maintain reasonably good accuracy when there is rain in the field of view. The rms difference between the SSM/I water vapor retrieval and radiosondes is about 5 mm for rain rates from 1 to 15 mm/h. Errors in the water vapor retrievals appear to be uncorrelated with the rain rate. This indicates that the algorithm is successfully orthogonalizing the retrievals so that there is a minimum of cross-talk between the retrieved parameters.

As expected the effective radiating temperature T_U exhibits a strong depression relative to the mean air temperature for moderate to heavy rain. This depression is due 1) to radiative scattering from large rain drops and ice and 2) to that fact that most of the radiation is coming from the cold top part of the rain cloud. For the heaviest rain, the T_U depression is -10 K and -20 K for 19 and 37 GHz, respectively.

The spectral signature of the retrieved τ_L shows that the ratio of the 37-GHz to 19-GHz liquid water absorption is, on the average, about 40% lower than predicted by Mie theory for moderate to heavy rain. We attribute this difference to the beamfilling effect, which we parameterize in terms of the normalized rms variation β of the liquid water absorption A_L. To correct for this effect, the 37-GHz to 19-GHz liquid water absorptions are increased until the Mie ratio is realized. Globally, we find the normalized rms variation of A_L to be about 0.85, which is somewhat less than that for an exponential pdf. Of course, individual observations can have values of β substantially higher than 0.85.

The last step in the rain rate retrieval involves dividing the columnar rain rate by some assumed rain column height H. In the tropics, we find using the freezing level, which is about 5 km, to specify H results in tropical rain rates that appear to be to low when compared with other rainfall climatologies. This low bias may be due to a substantial portion of the rain in the tropics not extending all the way to the freezing level (Fletcher, 1969). To correct the low bias, we use a value of H ~ 3 km in the tropics.

Global rain rates are produced for the 1991 through 1994 period from two SSM/I's that are aboard the F10 and F11 satellites. The probability density function (pdf) for the retrieved rain rates (averaged over the 32 km SSM/I footprint) shows that on a global basis 6% of the SSM/I observations detect measurable rain rates (R > 0.2 mm/h). One-half of the total global oceanic rainfall occurs at footprint-averaged rates above (and below) about 3.5 mm/h. For rainfall in the tropics, this value increases to 5.5 mm/h. Globally, the average rainfall over the oceans is about 2.9 mm/day, and in the tropics (20 N to 20 S) it is 3.9 mm/day. Zonal averages and global maps of the retrieved rain rates show structures that are similar to those in previously published rain climatologies. The peak at the ITCZ is quite narrow in meridional extent and varies from about 7 mm/day in the winter to a maximum 11 mm/day in the summer. Very low precipitation rates (< 0.3 mm/day) are observed in those areas of subsidence influenced by the large semipermanent anticylones.

We compare our rainfall estimates (WS) to two other emission-based rain satellite climatologies: Spencer (1993; MSU) and Wilheit *et al.* (1991; WCC). The agreement is reasonably good. In the ITCZ, the WS, MSU, and WCC reach maximum values of 8.1, 7.4, and 6.9 mm/day, respectively. In the extratropics storm track regions, the situation reverses, with the WS rainfall as the lowest, and MSU as the highest. Very close agreement is seen in the very dry areas associated with the semipermanent anticylones. The largest differences are seen between the MSU and WS. In the downstream portions of the extratropical storm tracks, the MSU rain is significantly greater than the WS. In contrast, the MSU rainfall is less over most portions of the tropics, particularly in the tropical west Pacific. The MSU minus WS rain difference seems to be related with cloud water. Areas where the MSU-WS difference is significantly positive (negative) are moderately correlated with areas having a relatively high (low) cloud amount as compared to the rainfall.

In conclusion, there still remains the problem of absolutely calibrating the rain algorithm. The lack of good-quality *in situ* rain measurements over the oceans has been a major source of difficulty for all satellite-based rainfall estimation techniques, and it is still not clear how to best deal with the calibration problem. Hopefully future programs such as TRMM and the Precipitation Intercomparison Project (PIP) will contribute to the better calibration of rainfall derived from satellites.

REFERENCES

Buettner, K.J.K., 1963: Regenortung vom wettersatelliten mit hilfe von zentimeterwellen (Rain localization from a weather satellite via centermeter waves). *Naturwiss*., **50,** 591.

Fletcher, N.H., 1969: *The Physics of Rainclouds*. Cambridge University Press, New York, NY, 390pp.

Goldstein, H., 1951: Attenuation by condensed water. *Propagation of Short Radio Waves*, MIT Rad. Lab. Ser*.,* 13, McGraw-Hill, New York.

Hollinger, J., R. Lo, G. Poe, R. Savage, and J. Pierce, 1987: Special Sensor Microwave/Imager User's Guide. *NRL Tech. Rpt.,* Naval Research Laboratory, Washington, DC. 120 pp.

Jones, D.M.A., and A.L. Sims, 1978: Climatology of instantaneous rainfall rates. *J. Appl. Meteor*., **17**, 1135-1140.

Petty, G. W., 1994: Physical retrievals of over-ocean rain rate from multichannel microwave imagery. Part I: Theoretical characteristics of normalized polarization and scattering indices. *Meteorol. Atmos. Phys.,* **54**, 79-99.

Shea, D.J., K.E. Trenberth, and R.W. Reynolds, 1990: A global monthly sea surface temperature climatology. *NCAR Tech. Note 345,* National Center for Atmospheric Research, 167 pp.

Simpson, J., R.F. Adler, and G.R. North, 1988: A proposed Tropical Rainfall Measuring Mission (TRMM) satellite. *Bull. Amer. Meteor. Soc*., **69**, 278-295.

Spencer, R.W., 1986: A satellite passive 37 GHz scattering-based method for measuring oceanic rain rates. *J. Climate Appl. Meteor*., **25**, 754-766.

Spencer, R.W., 1993: Global oceanic precipitation from the MSU during 1979-92 and comparisons to other climatologies. *J. Climate*, **6**, 1301-1326.

Spencer, R.W., H.M. Goodman, and R.E. Hood, 1989: Precipitation retrieval over land and ocean with the SSM/I: identification and characteristics of the scattering signal. *J. Atmos. Oceanic Tech*., **6**, 254-273.

Wentz, F.J., 1990: SBIR Phase II Report: West coast storm forecasting with SSM/I, *RSS Tech. Rpt. 033190*, Remote Sensing Systems, Santa Rosa, Ca, 378 pp.

Wentz, F.J., 1991: User's manual: SSM/I antenna temperature tapes, revision 1, *RSS Tech. Rpt. 120191,* Remote Sensing Systems, Santa Rosa, CA, 69 pp.

Wentz, F.J., 1995: A well-calibrated ocean algorithm for SSM/I. (Submitted to J. Geophy. Res.)

Wilheit, T.T., A.T.C. Chang, M.S.V. Rao, E.B. Rodgers, and J.S. Theon, 1977: A satellite technique for quantitatively mapping rainfall over the oceans. *J. Appl. Meteor*., **16**, 551-560.

Wilheit, T.T., A.T.C. Chamg, and L.S. Chiu, 1991: Retrieval of monthly rainfall indices from microwave radiometric measurements using probability distribution functions. *J. Atmos. Oceanic Tech*., **8**, 118-136.